Hierarchical flower-like SnSe$_2$ supported Ag$_3$PO$_4$ nanoparticles: Towards visible light driven photocatalyst with enhanced performance

Pengfei Tan, Xi Chen, Laidi Wu, Yan Yang Shang, Wenwen Liu, Jun Pan*, Xiang Xiong

State Key Laboratory for Powder Metallurgy, Central South University, Changsha 410083, PR China

ABSTRACT

A novel three-dimensional (3D) hierarchical flower-like Ag$_3$PO$_4$/SnSe$_2$ composite photocatalyst was successfully prepared via an in situ precipitation method. The composition, microstructure and optical properties of the Ag$_3$PO$_4$/SnSe$_2$ composites were thoroughly investigated. Nano-sized Ag$_3$PO$_4$ particles were uniformly dispersed on the surface of 3D flower-like SnSe$_2$. The obtained Ag$_3$PO$_4$/SnSe$_2$ composites presented enhanced performance for photocatalytic degradation of Rhodamine B (RhB) compared with pure Ag$_3$PO$_4$ and SnSe$_2$ under visible light irradiation. The Ag$_3$PO$_4$/SnSe$_2$-6 composite exhibited the optimal efficiency for photocatalytic decomposition of RhB, approximately 4.2 and 26 times higher than those of pure Ag$_3$PO$_4$ and SnSe$_2$. Significantly, the superior stability was also observed after four cycles. The enhanced performance of the Ag$_3$PO$_4$/SnSe$_2$ composites under visible light was ascribed to a synergistic effect including the matched energy band structures, increased light harvesting and boosted separation efficiency of photo-generated carriers. A possible photocatalytic mechanism of the composite was also discussed.

© 2016 Elsevier B.V. All rights reserved.

1. Introduction

Degradation of organic pollutants in water by the utilization of free and green solar energy in the presence of semiconductor photocatalysts has been regarded as a promising and sustainable way to solve environmental pollution [1–3]. Unfortunately, most widely used photocatalysts are just active under the UV-light irradiation only occupying 5% of the total sunlight energy, which seriously restricts their practical applications under sunlight [4–6]. Consequently, it's urgent to develop novel efficient visible light driven photocatalysts.

Recently, numerous Ag-based photocatalysts such as Ag$_3$PO$_4$ [7], AgVO$_3$ [8], Ag$_2$CO$_3$ [9] and Ag$_2$CrO$_4$ [10], have been extensively investigated because of their response to visible light. Among them, Ag$_3$PO$_4$ has earned particular attention owing to its strong optical absorption, low-toxicity, excellent quantum efficiency and the high activity in the photodecomposition of organic contaminants under visible light [1,11–14]. Nevertheless, its practical applications as photocatalyst are still restricted by some severe drawbacks such as aggregation and photocorrosion as well as the limited visible light

responsive range. Many studies were proposed to improve its performance in photocatalytic degradation efficiency [15–21]. One of the effective ways is to build composite structures by assembling Ag$_3$PO$_4$ with other semiconductors such as CeO$_2$ [22], Nb$_2$O$_5$ [23], Ta$_3$N$_5$ [24], GO [25] etc. In those systems, the composites exhibited a better photocatalytic performance compared with the pure Ag$_3$PO$_4$ and the enhanced photocatalytic activity is attributed to the synergistic effect including the matched bandgap structures, the improved visible light absorption and the enhanced separation rates of photogenerated electron-hole pairs.

With proper band structure, two-dimensional layered materials, such as MoS$_2$ [26,27], Ag$_2$S [24,28] and g-C$_3$N$_4$ [29–31], have been reported as supporters to enhance the degradation efficiency and stability of Ag$_3$PO$_4$. As one kind of these layered materials, tin selenides (SnSe$_2$), a n-type semiconductor with a narrow band gap of 1.28 eV [32], has been intensively applied to the fields of energy storage, solar cell and optoelectronics [33–38]. However, as far as we know, its photocatalytic performance is rarely studied. In consideration of the suitable band structure and the desired band gap, it has great potential in environmental remediation and improving the photocatalytic activity of Ag$_3$PO$_4$. Moreover, the unique 3D hierarchical flower-like structure has been proved to have more excellent photocatalytic performance due to higher specific surface area, more active sites and enhanced light harvesting

---

[39–43]. Thus, in present study, $SnSe_2$ with 3D hierarchical flower-like structure was prepared to support Ag_3PO_4 nanoparticles. On one hand, the dispersity of Ag_3PO_4 is very likely to be improved by the 3D hierarchical $SnSe_2$ acting as clapboards to separate Ag_3PO_4 nanoparticles. On the other hand, because of the superior optical property of $SnSe_2$ and the matched energy position between Ag_3PO_4 and $SnSe_2$, the architecture of this composite is expected to enhance the separation rates of electron-hole pairs, improve the visible-light absorption and promote the stability of Ag_3PO_4.

Motivated by the foregoing discussion, a novel high efficiency 3D hierarchical $Ag_3PO_4/SnSe_2$ composite photocatalyst was synthesized for the first time via a facile in situ template-free precipitation method. Structure characterizations demonstrate that Ag_3PO_4 nanoparticles were uniformly grown on the surface of 3D hierarchical $SnSe_2$. Degradation tests of RhB under visible light irradiation were conducted to confirm the superiority of this composite. Finally, on the basis of the experimental results, the photocatalytic mechanism of this composite was also proposed.

2. Experimental section

2.1. Materials

All the reagents in this work used were analytical grade and used without further purification.

2.2. Preparation of photocatalysts

2.2.1. Preparation of 3D hierarchical flower-like SnSe₂

The 3D hierarchical flower-like $SnSe_2$ were prepared following the reported method [32]. Typically, 0.2 mmol of $SnCl_4·5H_2O$, and 0.2 mmol of SeO_2 were added to 17 mL of oleylamine followed by the addition of 500 μL of oleic acid. The mixture was heated at 70 °C for 30 min. Then, the obtained mixture was transferred to a 25 mL Teflon-lined autoclave and heated to 180 °C for 36 h. After the autoclave was cooled down to room temperature, the resulting precipitate was washed with a toluene and ethanol mixture (1:2) three times, and dried at 60 °C for 8 h.

2.2.2. Preparation of Ag₃PO₄/SnSe₂ composites

Ag_3PO_4 nanoparticles coupled with different amounts of $SnSe_2$ were prepared through a facile in situ growth method in an organic solvent. Firstly, 0.17 g of silver nitrate and 8.2 mL of oleylamine were dissolved in 30 mL of toluene. An appropriate amount of the prepared $SnSe_2$ was dispersed in a solution of ethanol (10 mL) by ultrasonic treatment for 10 min, and then 0.067 mL of phosphoric acid solution (85 wt.%) was added to the obtained solution under magnetic stirring. Next, the above mixed solution of $SnSe_2$ and phosphoric acid was gradually added to the obtained toluene solution of silver nitrate and oleylamine under stirring. After stirring for 1 h, excess ethanol was added to precipitate $Ag_3PO_4/SnSe_2$ composites. The obtained $Ag_3PO_4/SnSe_2$ composites were collected and washed with toluene and absolute alcohol, then dried in vacuum at 60 °C for a whole night. The as-prepared products were named as $Ag_3PO_4/SnSe_2$-X (X was denoted the theoretical weight ratio of $SnSe_2$ in the $Ag_3PO_4/SnSe_2$ composite, the accurate weight percentage of $SnSe_2$ in the composites were given in Table S1). The pure Ag_3PO_4 were also prepared for comparison following the same method without the addition of $SnSe_2$.

2.3. Characterization of the as-prepared photocatalysts

The crystal structures of the composites were tested by X-ray diffraction (D/max 2550, Rigaku Corporation). The morphologies of the as-prepared samples were examined by emission scanning microscopy (Nova Nano SEM 230, FEI Electron Optics B.V) and field

emission transmission electron microscopy (JEM-2100F, Japanese electronics co. LTD). XPS analysis was performed on an ESCALab MKII X-ray photoelectron spectrometer using Mg-Kα radiation. The Brunauer-Emmett-Teller (BET) surface area test was performed on a TRISTAR-3000 surface area analyzer. The total organic carbon (TOC) assays were tested using a Shimadzu TOC-VCPH analyzer. The photoluminescence (PL) spectra were measured on a fluorescence spectrophotometer (F-4600, Japan's Hitachi LTD). The UV–vis spectra of the catalysts were obtained on a UV–vis spectrometer (Evolution 220, Thermo Fisher Scientific). The samples for electron spin resonance (ESR) measurement were prepared by mixing the as-prepared samples in a 50 mM DMPO solution tank (aqueous dispersion for DMPO-•OH and methanol dispersion for DMPO-•O_2^-,λ >420 nm visible light irradiation).

2.4. Photoelectrochemistry measurement

The photocurrent and the electrochemical impedance spectra (EIS) of the photocatalysts were obtained using an electrochemical workstation (CHI 660e, China). A standard three-electrode system was performed in this photochemical study. The platinum plate was served as a counter electrode and a standard calomel electrode as a reference electrode. 0.1 M sodium sulfate aqueous solution was acted as electrolyte. The working electrodes were manufactured as follows: 12 mg photocatalysts were dispersed in 500 μL ethanol with 20 μL 5 wt% Nafion aqueous solution and ultrasonication 30 min to form a homogeneous suspension. Then, 60 μL above suspension was dropped onto the surface of 1 cm × 1 cm indium tin oxide (ITO) glass. Subsequently, the ITO coated with photocatalysts annealed for 2 h in air at 200 °C. The EIS was implemented at 5 mV amplitude and frequency range of 1000 kHz to 0.1 Hz.

2.5. Photocatalytic activity test

The photocatalytic activity of the samples was evaluated under a 300 W Xe lamp with a 400 nm cutoff filter [44,45]. In every experiment, 10 mg of the photocatalyst was placed in a quartz tube containing 15 mL of RhB solution (10 mg L^{-1}). Prior to irradiation, the suspension was magnetically stirred for 30 min in the dark to ensure that the RhB could reach adsorption/desorption equilibrium on the photocatalyst surface. After irradiation, 3 mL of the solution was suctioned at a regular time interval and centrifuged to remove the precipitates, then the concentrations of RhB in the supernatant was determined by a UV–vis spectrophotometer at a wavelength of 554 nm. The trapping experiments concerning active species in the photocatalytic process were also conducted by adding the different scavengers into the RhB solution prior to the photocatalyst in the similar procedure.

3. Results and discussion

3.1. Structure characterizations of photocatalysts

XRD patterns of pure Ag_3PO_4, $SnSe_2$ and $Ag_3PO_4/SnSe_2$ composites were shown in Fig. 1. For pure Ag_3PO_4, all the appeared diffraction peaks could be assigned to the cubic phase of Ag_3PO_4 (JCPDS: 06-0505). The intensity and the diffraction peaks of Ag_3PO_4 improved that it possessed a high degree of crystallinity. As for the $SnSe_2$ sample, all the peaks were respectively corresponding to the $SnSe_2$ phase (JCPDS: 89-3197). It is clear that the $Ag_3PO_4/SnSe_2$ composites exhibited similar XRD patterns to pure Ag_3PO_4 indicating the introduction of $SnSe_2$ did not change the lattice of Ag_3PO_4. It is worth mentioning that no obvious diffraction peaks of $SnSe_2$ were detected in the composites due to the low content. The following results of XPS and SEM could further identify the existence of $SnSe_2$.
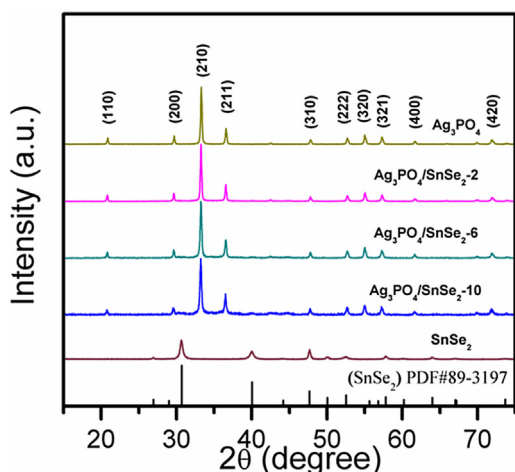
Fig. 1. XRD patterns of Ag_3PO_4, $SnSe_2$, and $Ag_3PO_4/SnSe_2$-X composites.

XPS was carried out to further investigate the composition and chemical status of the $Ag_3PO_4/SnSe_2$-6 composite, and the results were shown in Fig. 2. All the peaks ascribed to Ag, P, O, Sn and Se elements were detected in the XPS survey spectrum (Fig. 2a) and no peaks corresponding to other elements were observed. The high resolution spectra of each elements were shown in Fig. 2b-f. There were two individual peaks at 374.0 and 368.0 eV in Fig. 2b, which could be assigned to $3d_{3/2}$ and $3d_{5/2}$ of Ag^+ respectively [46]. In Fig. 2c, the P 2p peak was at 132.8 eV, which corresponds to P^{5+} coming from Ag_3PO_4 [47]. For the O 1s XPS spectra shown in Fig. 2d, the binding energy of 530.6 eV was attributed to the O^{2-} in the Ag_3PO_4, while the peak at 532 eV probably corresponded to the hydroxyl group [29]. Regarding the Sn 3d spectra displayed in Fig. 2e, two kinds of binding energies located at 494.7 and 486.3 eV could be respectively attributed to Sn $3d_{3/2}$ and $3d_{5/2}$, implying that Sn was in the form of Sn^{4+} oxidation state [48]. The Se 3d high resolution XPS spectrum could be fitted into two peaks at 54.4 and 53.6 eV, as revealed in Fig. 2f, which were separately belonging to Se $3d_{3/2}$ and Se $3d_{5/2}$, suggesting that Se was in the form of Se^{2-} [36]. The XPS spectra of Sn 3d and Se 3d indicated the existence of $SnSe_2$ in the composites.

The morphologies of pure $SnSe_2$, Ag_3PO_4 and the as-prepared $Ag_3PO_4/SnSe_2$-6 composite were observed via SEM and TEM. The SEM images of pure $SnSe_2$ (Fig. 3a, b) indicated that the $SnSe_2$ possessed 3D flower-like structures (with diameters of 3–5 μm), which were composed of several thin sheets. It was clearly observed
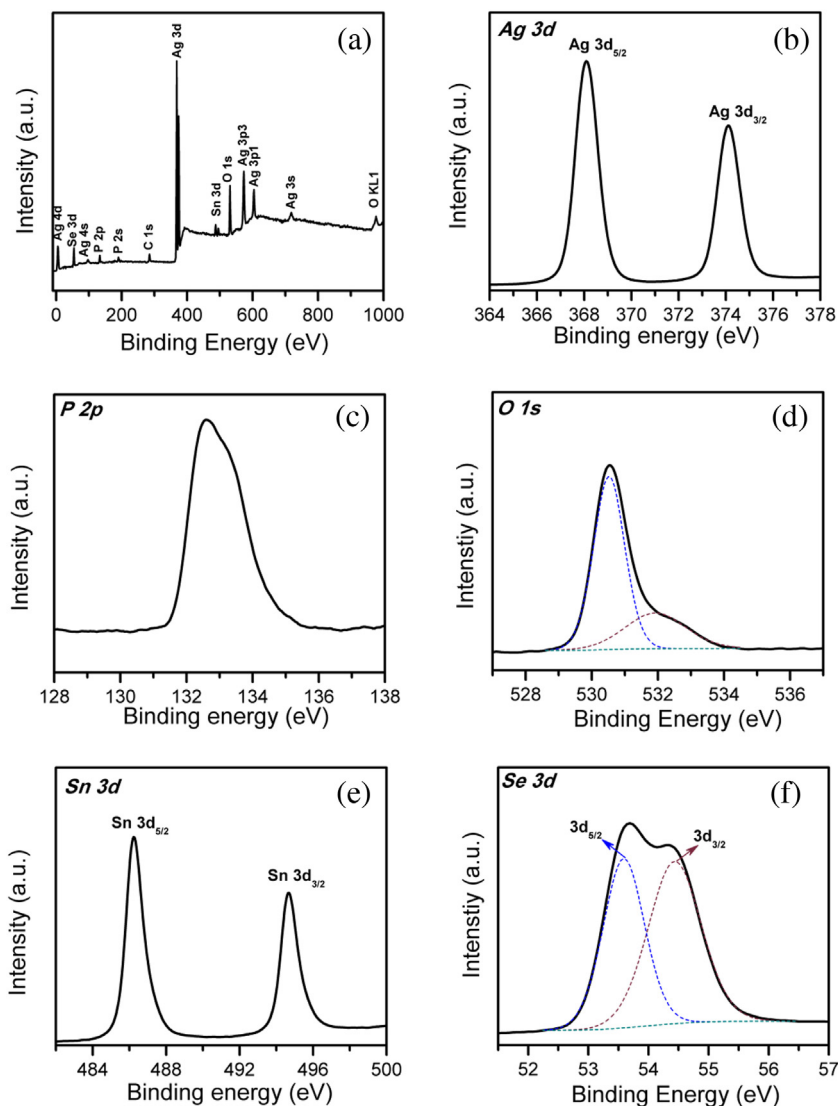

Fig. 2. XPS spectra of $Ag_3PO_4/SnSe_2$ composites: (a) survey spectra, (b) Ag 3d, (c) P 2p, (d) O 1s, (e) Sn 3d and (f) Se 3d.

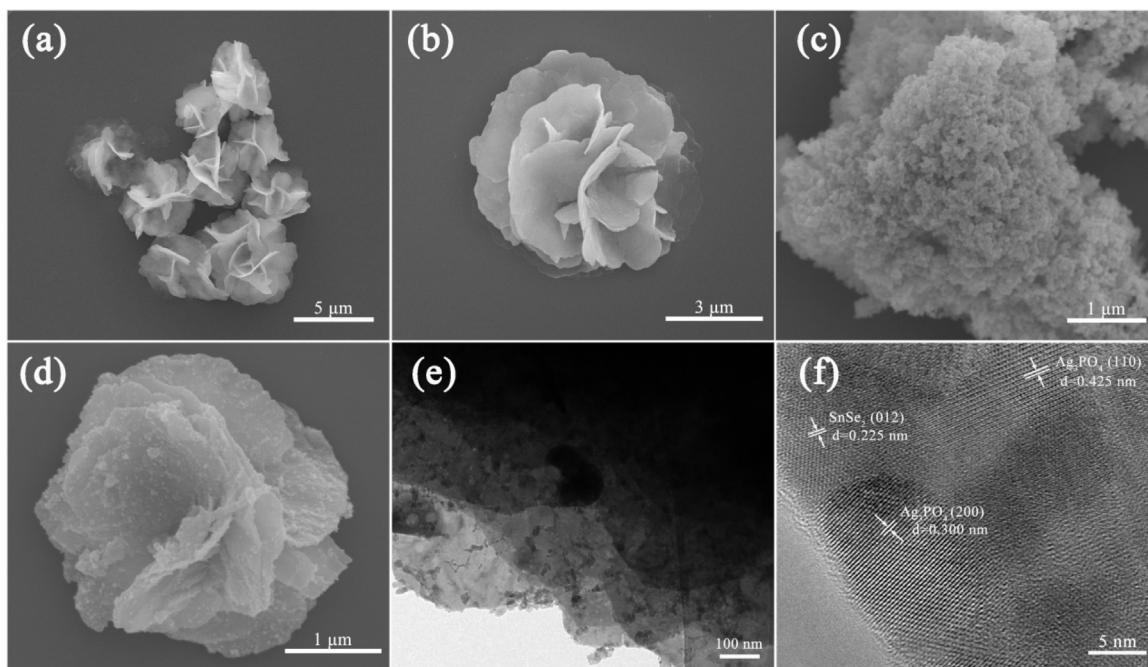**Fig. 3.** SEM images of the (a,b) $SnSe_2$, (c) Ag_3PO_4, and (d) $Ag_3PO_4/SnSe_2$-6, TEM image of (e) $Ag_3PO_4/SnSe_2$-6 and HRTEM image (f) of $Ag_3PO_4/SnSe_2$-6.

that Ag_3PO_4 particles with the size of 40–80 nm were seriously agglomerated (Fig. 3c). A typical SEM image of the as-prepared $Ag_3PO_4/SnSe_2$-6 composite was seen from Fig. 3d. The Ag_3PO_4 nanoparticles were homogeneously dispersed on surface of the 3D hierarchical flower-like $SnSe_2$. After deposition of Ag_3PO_4, the morphology of $SnSe_2$ was maintained. Moreover, the aggregation of Ag_3PO_4 was significantly alleviated, and its particle size was also decreased. The compellent reason is that the nanosheets building the special 3D hierarchical flower-like $SnSe_2$ could act as clapboards to separate Ag_3PO_4 nanoparticles effectively. The corresponding fine microstructure of the $Ag_3PO_4/SnSe_2$-6 composite was investigated by TEM. As shown in Fig. 3e, Ag_3PO_4 nanoparticles were observed to adhere to the surface of $SnSe_2$. The HRTEM image (Fig. 3f) of the sample showed the distinct crystallographic planes of Ag_3PO_4 and $SnSe_2$, in which a lattice spacing of 0.225 nm corresponded to the (012) plane of the hexagonal $SnSe_2$ phase and the lattice spacings of 0.425 and 0.300 nm corresponded to the (110)

and (200) planes of the cubic Ag_3PO_4 phase. The above discussion demonstrated the composite was consisted of $SnSe_2$ and Ag_3PO_4.

The BET specific surface area and pore structure of the as-prepared samples were investigated by nitrogen adsorption–desorption measurements. As can be seen in Fig. 4, the results showed that all samples possessed a type IV isotherm, suggesting the presence of mesopores[49]. The specific surface areas of pure $SnSe_2$, Ag_3PO_4 and $Ag_3PO_4/SnSe_2$-6 composite were 11.398 m^2/g, 4.886 m^2/g and 22.763 m^2/g, respectively (Table S1). The increase of surface areas of $Ag_3PO_4/SnSe_2$-6 was induced by the addition of 3D hierarchical $SnSe_2$ structures and the relatively better dispersion of Ag_3PO_4 nanoparticles, which can be evidenced by SEM. The high surface area was one of the factors that influenced the photocatalytic performance of composites under visible light irradiation.

3.2. Optical absorption properties

To investigate the optical properties of the as-prepared samples, UV–vis diffuse reflectance spectra of $SnSe_2$, Ag_3PO_4, and $Ag_3PO_4/SnSe_2$ composites were recorded. It can be observed that pure Ag_3PO_4 exhibits a sharp fundamental absorption edge at about 530 nm in Fig. 5. The $SnSe_2$ with a narrow band gap display a strong absorption from ultraviolet region to visible region. Obviously, the $Ag_3PO_4/SnSe_2$ composites showed enhanced visible light response with increasing the content of $SnSe_2$. Besides, the absorption of $Ag_3PO_4/SnSe_2$ shifted to longer wavelengths as the content of $SnSe_2$ increased. It was also observed that the color of the samples changed from yellow to gray when more black $SnSe_2$ was introduced. Therefore, the introduction of narrow gap $SnSe_2$ could improve the light harvesting efficiency of Ag_3PO_4 in the visible light region, and then produced more photogenerated electron–hole pairs to participate in the degradation process, which would be favorable for the photocatalytic activity [50].

3.3. Photocatalytic activities of $Ag_3PO_4/SnSe_2$ composites

The photocatalytic activities of pure Ag_3PO_4, $SnSe_2$, and different ratios of $Ag_3PO_4/SnSe_2$ composites were measured by the
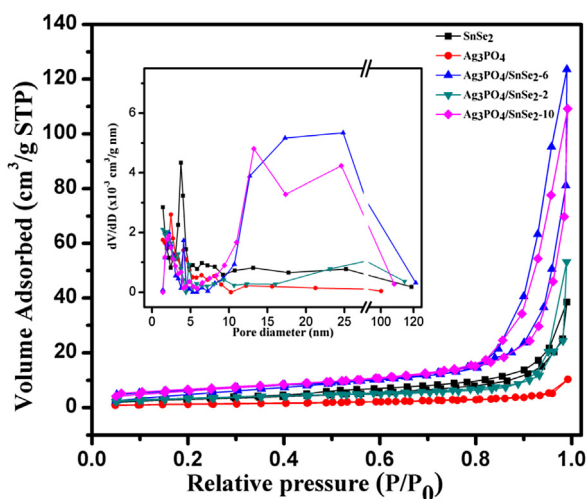

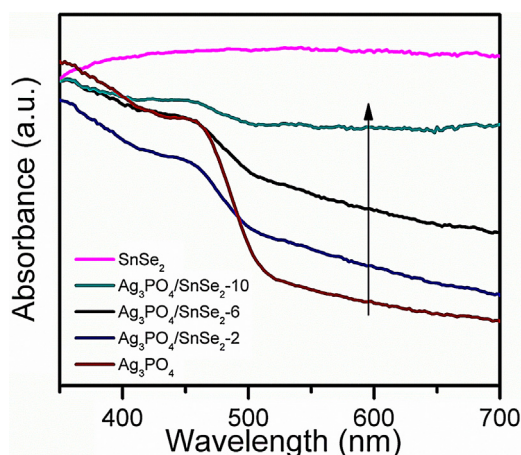**Fig. 4.** N_2 adsorption–desorption isotherms and pore size distribution (inset) of the samples.

Fig. 5. UV–vis diffuse reflectance spectra of pure Ag$_3$PO$_4$, SnSe$_2$ and Ag$_3$PO$_4$/SnSe$_2$ composites with different contents of SnSe$_2$.

photodegradation of RhB in an aqueous solution. Prior to visible light irradiation, the reaction mixture was magnetically stirred in darkness for 30 min to ensure the adsorption/desorption equilibrium between dyes and photocatalysts. As shown in Fig. 6A, the self-degradation of RhB was almost negligible in the absence of photocatalyst. After irradiation for 50 min, the efficiencies of the degradation for RhB were 14.1% and 58.7% for bare SnSe$_2$ and pure Ag$_3$PO$_4$, respectively. Excitingly, all the Ag$_3$PO$_4$/SnSe$_2$ nanocomposites showed enhanced photocatalytic performances than pure Ag$_3$PO$_4$ and SnSe$_2$. The photocatalytic performance was significantly improved after the introduction of SnSe$_2$ and increased with the increase of SnSe$_2$ content from 2.0 to 6.0 wt.%. For example, the Ag$_3$PO$_4$/SnSe$_2$-6 exhibited the highest activity, approximately 100% of the RhB was decomposed from the solution. Further

increasing the SnSe$_2$ content to 10 wt.% in the composite leads to a decreased photocatalytic activity. The photocatalytic activities of the samples depended on the mass ratio of Ag$_3$PO$_4$ and SnSe$_2$, indicating the amount of SnSe$_2$ was crucial to the synergistic effect between SnSe$_2$ and Ag$_3$PO$_4$. This may be harmful to light harvesting if SnSe$_2$ was little, while too much SnSe$_2$ would impede the light from contacting Ag$_3$PO$_4$ nanoparticles and perhaps cover the partial reactive sites of Ag$_3$PO$_4$ nanoparticles, which was not benefit for the carriers separation. It is reasonable that Ag$_3$PO$_4$/SnSe$_2$-6 exhibited the optimal activity in consideration of both charge separation and light absorption. The absorption changes for RhB solution in the presence of Ag$_3$PO$_4$/SnSe$_2$-6 were shown in Fig. 6D. With increasing irradiation time, the absorption peak of RhB was decreased gradually and nearly 100% of RhB could be degraded after irradiation for 50 min.

Moreover, the photocatalytic degradation kinetics curves of RhB in the presence of different samples were shown in Fig. 6B. All of them were linear and the curves followed the pseudo-first-order kinetic model $ln(C_0/C) = kt$, where k is the apparent kinetic rate constants, t is the reaction time, C and C_0 are the concentration at t and the initial concentration of the organic dyes, respectively. The apparent rate constants were 0.283% min^{-1}, 1.727% min^{-1}, 2.171% min^{-1}, 4.207% min^{-1}, 7.237% min^{-1} and 3.225% min^{-1} for SnSe$_2$, Ag$_3$PO$_4$, Ag$_3$PO$_4$/SnSe$_2$-2, Ag$_3$PO$_4$/SnSe$_2$-4, Ag$_3$PO$_4$/SnSe$_2$-6 and Ag$_3$PO$_4$/SnSe$_2$-10 respectively (Fig. 6C). It could be clearly seen that the rate constant of Ag$_3$PO$_4$/SnSe$_2$-6 was highest, which was almost 26 times higher than that of SnSe$_2$ and 4.2 times higher than that of Ag$_3$PO$_4$. Meanwhile, the TOC removal efficiencies of the as-prepared samples were also determined. As seen from Fig. S1, their TOC removal efficiencies gradually increase with prolonging the illumination time. After 50 min irradiation, a mineralization rate of 34.72% and 72.12% for pure Ag$_3$PO$_4$ and Ag$_3$PO$_4$/SnSe$_2$-6 composite, suggesting higher mineralization ability was achieved by the modified Ag$_3$PO$_4$ [51].
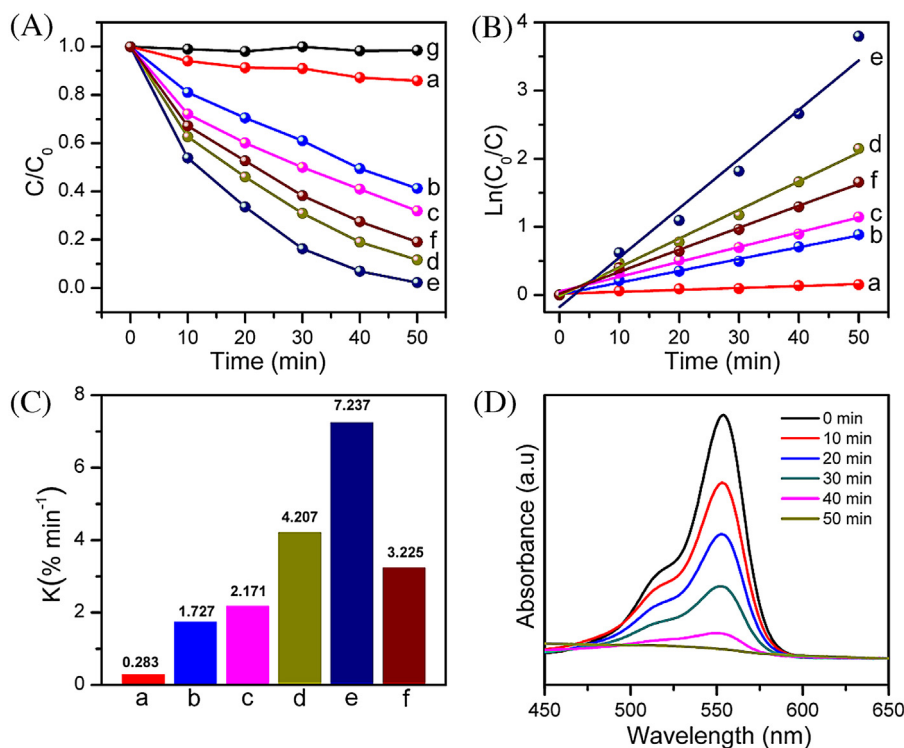

Fig. 6. (A) The photocatalytic activity of the samples for RhB solution, (B) the kinetics plots of RhB degradation over the as-synthesized photocatalysts, (C) the apparent rate constant over all samples for degradation of RhB and (D) the absorption spectral changes of RhB in the presence of the sample Ag$_3$PO$_4$/SnSe$_2$-6. (a) SnSe$_2$, (b) Ag$_3$PO$_4$, (c) Ag$_3$PO$_4$/SnSe$_2$-2, (d) Ag$_3$PO$_4$/SnSe$_2$-4, (e) Ag$_3$PO$_4$/SnSe$_2$-6, (f) Ag$_3$PO$_4$/SnSe$_2$-10, (g) without any catalyst.
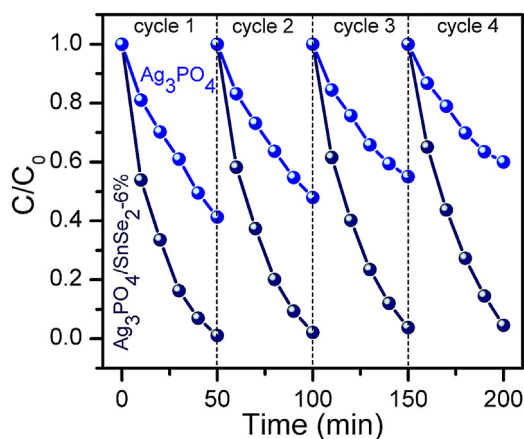
Fig. 7. Cyclic performance of Ag$_3$PO$_4$/SnSe$_2$-6 and Ag$_3$PO$_4$ for the degradation of RhB under visible light irradiation.

3.4. Cycling experiments

Apart from photocatalytic efficiency, the stability of photocatalysts is another key issue from the view of practical application. The recycle experiments for RhB degradation under visible light irradiation were conducted in the presence of pure Ag$_3$PO$_4$ and Ag$_3$PO$_4$/SnSe$_2$-6. As presented in Fig. 7, the degradation efficiency of pure Ag$_3$PO$_4$ decreased from 60% to 40% after four successive cycles, while the photocatalytic activity of the Ag$_3$PO$_4$/SnSe$_2$-6 composite was effectively maintained except for 3% decrease from 99% to 96% after four cycling reactions. To further understand the stability of the samples, the XRD patterns and the Ag 3d XPS spectra of pure Ag$_3$PO$_4$ and Ag$_3$PO$_4$/SnSe$_2$-6 after four cycle experiments were measured. As shown in Fig. 8a, a weak peak assigned to metal-

lic Ag^0 at 38.1° appeared in the XRD pattern of pure Ag$_3$PO$_4$ after four cycles. In contrast, no evident metallic Ag^0 was detected in the Ag$_3$PO$_4$/SnSe$_2$-6 composite. These results clearly confirmed that the structural stability of Ag$_3$PO$_4$/SnSe$_2$-6 was significantly better than that of Ag$_3$PO$_4$. The Ag chemical statuses of Ag$_3$PO$_4$ and Ag$_3$PO$_4$/SnSe$_2$-6 were also investigated. For Ag$_3$PO$_4$, the peaks at 367.8 and 373.8 eV corresponded to the binding energies of Ag 3d$_{3/2}$ and Ag 3d$_{5/2}$ of Ag$^+$, whereas the peaks at 368.5 and 374.3 eV were attributed to the metallic Ag^0 (Fig. 8b). Fig. 8c showed two peaks of Ag$_3$PO$_4$/SnSe$_2$-6 at 368.0 and 374.0 eV belonging to Ag$^+$, and other two peaks at 368.5 and 374.2 eV ascribing to Ag^0. The slight peak shifts were mainly attributed to the interaction between Ag$_3$PO$_4$ and SnSe$_2$. It was obvious that much less metallic Ag was formed in Ag$_3$PO$_4$/SnSe$_2$-6 and the photocorrosion of Ag$_3$PO$_4$ could be significantly inhibited by introducing of SnSe$_2$. The reason could be explained as follows: when the SnSe$_2$ was introduced as the support of Ag$_3$PO$_4$, the photogenerated electrons formed on the conduction band (CB) of the Ag$_3$PO$_4$ could migrate quickly to the valence band (VB) of SnSe$_2$ and combine with holes there, resulting in more efficient separation of the photogenerated carriers, and then the photocorrosion of the Ag$_3$PO$_4$ could be suppressed to some extent. These have been reported by many researchers [52,53]. In addition, after four cycles, the spectra of Sn 3d and Se 3d XPS in Ag$_3$PO$_4$/SnSe$_2$-6 composite shows no apparent shift compared with the sample before the reaction (Fig. S2), indicating the photocatalyst is stable in the photocatalytic reaction. In summary, compared with the pure Ag$_3$PO$_4$, the presence of the SnSe$_2$ improved the photocatalytic activity and stability of the composite.

3.5. PL and EIS spectra

It is well known that the photoluminescence emission spectra (PL) could be applied for the semiconductors to detect the processes
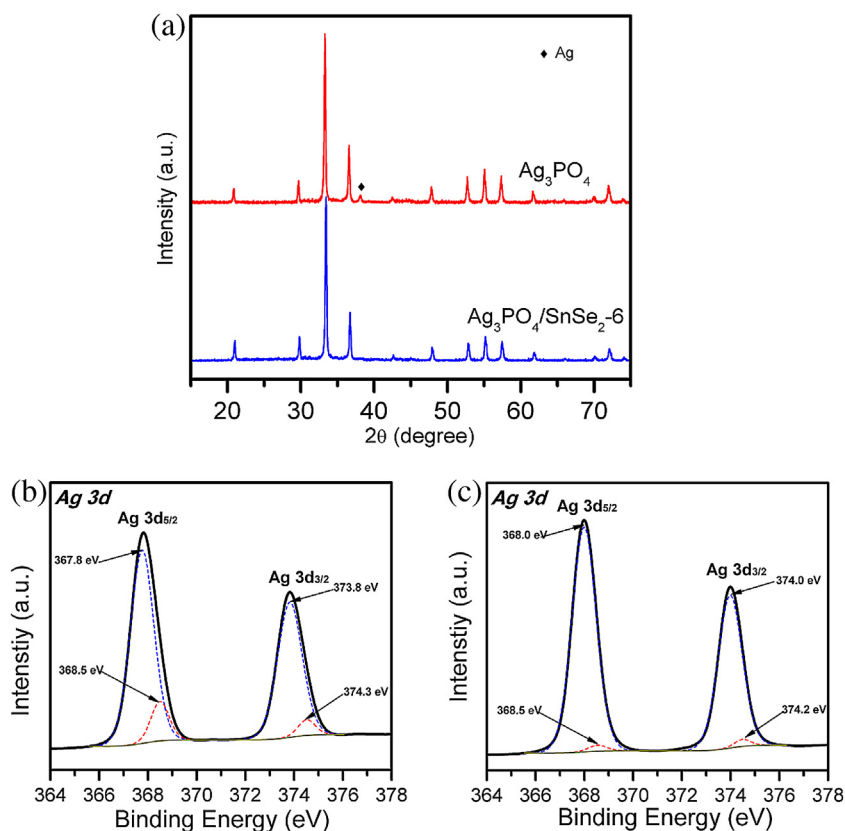

Fig. 8. (a) XRD patterns of Ag$_3$PO$_4$ and Ag$_3$PO$_4$/SnSe$_2$-6 after fourth cycle experiments; Ag 3d XPS spectra of (b) Ag$_3$PO$_4$ and (c) Ag$_3$PO$_4$/SnSe$_2$-6 after fourth cycle experiments.
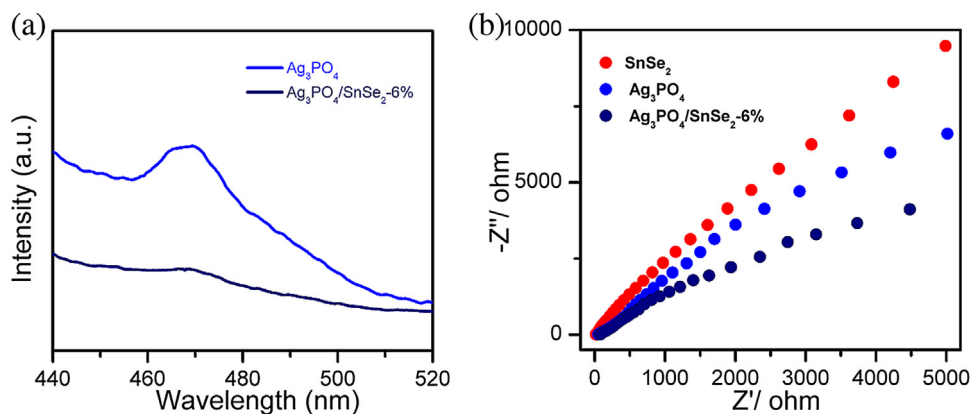
Fig. 9. (a) Photoluminescence spectra (PL) of Ag_3PO_4 and $Ag_3PO_4/SnSe_2$-6; (b) Electrochemical impedance spectroscopy (EIS) Nyquist plot of $SnSe_2$, Ag_3PO_4 and $Ag_3PO_4/SnSe_2$-6.

of the separation, transfer and recombination of the photogenerated electron–hole pairs. In general, a higher PL intensity of spectra means a higher recombination rate of photoinduced charge carriers [45,54,55]. As shown in Fig. 9a, the PL intensity of Ag_3PO_4 was higher than that of $Ag_3PO_4/SnSe_2$-6, which indicated that the recombination of photoexcited electron-hole pairs could be efficiently inhibited though the formation of this structure between Ag_3PO_4 and $SnSe_2$. In this study, EIS was also tested to characterize the interfacial charge transfer properties and the separation efficiency of the photogenerated carriers, where a smaller arc radius indicates higher efficiency in charge transfer [39]. As can be seen in Fig. 9b, the arc radius of $Ag_3PO_4/SnSe_2$-6 was smaller than that of Ag_3PO_4 or $SnSe_2$, indicating $Ag_3PO_4/SnSe_2$-6 had a higher interfacial charge transfer and a more effective separation of carriers. In addition, the photocurrent response of the as-obtained samples were recorded and depicted in Fig. 10. It's clear that, the photocurrent response of the $Ag_3PO_4/SnSe_2$-6 was much higher than that of the pure Ag_3PO_4 and $SnSe_2$ under the same condition, which means more efficient charge separation and migration. Therefore, the results of the PL, EIS and photocurrent response demonstrated that the introduction of $SnSe_2$ was effective to improve the charge separation and the transfer efficiency, resulting in the enhancement of the photocatalytic activity of Ag_3PO_4.

3.6. Detection of reactive oxidative species

In order to further determine the main active species involved in the degradation process and possible photodegradation mechanism, the trapping experiments of the composites were conducted. In this study, ethylenediamine tetraacetic acid disodium salt (EDTA-2Na, 5 mM), benoquinone (BQ, 5 mM) and *tert*-butyl alcohol (TBA, 5 mM) were employed as the scavengers for photo-generated holes (h^+), superoxide radical ($\bullet O_2^-$) and hydroxyl radical ($\bullet OH$), respectively [45,56]. As shown in Fig. 11, the degradation efficiency of RhB about $Ag_3PO_4/SnSe_2$-6 was slightly inhibited upon addition of TBA, implying that $\bullet OH$ played an insignificant role in the decomposition of RhB under visible light irradiation. In contrast, when EDTA or BQ was added, the photodegradation rates of RhB were distinctly suppressed, which indicate that the h^+ and $\bullet O_2^-$ were the major active species in the photocatalytic reaction process. As for pure Ag_3PO_4, the results (Fig.S3) certified that h^+ was the main oxidative species in the process, which was consistent with the previous literature[57]. Moreover, in order to further confirm the main active species in this photocatalytic system under visible irradiation, the ESR spin-trap with DMPO technique was performed on illuminated $Ag_3PO_4/SnSe_2$-6 composite (Fig.S4). The results of ESR were well consistent with the trapping experiments. Based on
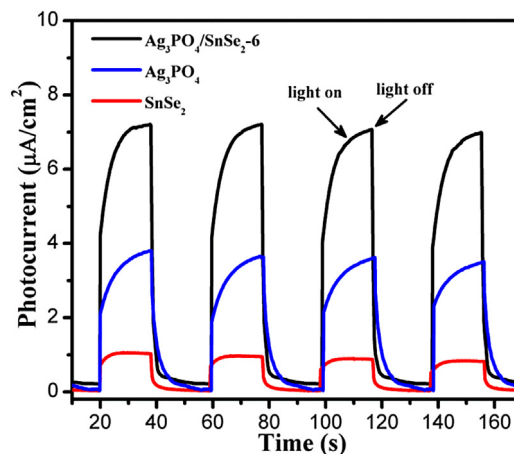

Fig. 10. Photocurrent response of the pure $SnSe_2$, Ag_3PO_4 and $Ag_3PO_4/SnSe_2$-6 composite under visible light irradiation.

the above results, it can be concluded that the degradation process occurring on the surface of $Ag_3PO_4/SnSe_2$-6 composite may involve the direct reaction of the pollutants with strong oxidizing superoxide radicals and holes. These results revealed that the photodegradation mechanism of $Ag_3PO_4/SnSe_2$-6 composite has been changed, if compared with that of pure Ag_3PO_4.

3.7. Photocatalytic mechanism

In order to thoroughly investigate the photcatalytic mechanism of the $Ag_3PO_4/SnSe_2$ composite, the conduction band (CB) and the valence band (VB) of $SnSe_2$ were estimated by the following equations [28]:

$$E_c = -\left(\chi(A)^a \cdot \chi(B)^b \cdot \chi(C)^c\right)^{1/(a+b+c)} + \frac{1}{2}E_g + E_0$$

$$E_v = E_c + E_g$$

where E_V is the valence band edge potential; χ is the electronegativity of the semiconductor, which is the geometric mean of the electronegativity of the constituent atoms; and E_0 is the energy of free electrons on the hydrogen scale (about 4.5 eV vs. NHE). For $SnSe_2$ and Ag_3PO_4, the values of Eg are 1.28 eV and 2.45 eV, respectively [32,53]. Therefore, the E_V potentials of $SnSe_2$ and Ag_3PO_4 were 1.12 eV and 2.9 eV, the E_C potentials were −0.16 eV and 0.45 eV, respectively.
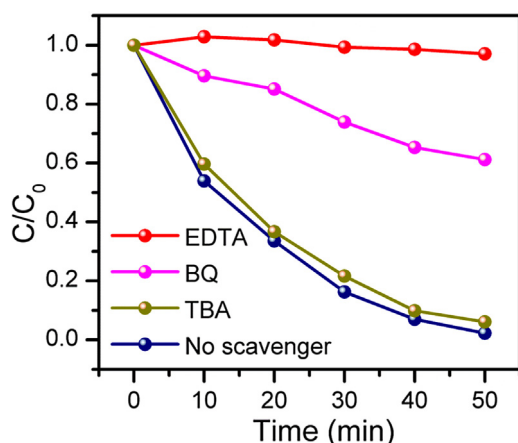
Fig. 11. Photocatalytic activities of the $Ag_3PO_4/SnSe_2$-6 composite for the degradation of RhB in the presence of different scavengers.
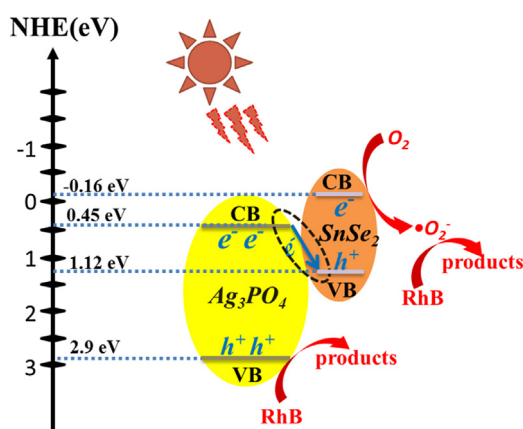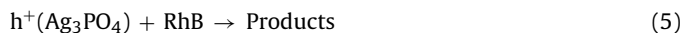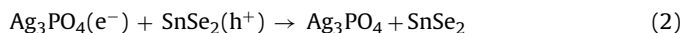

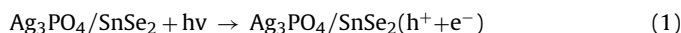**Fig. 12.** Schematic illustration of the photocatalytic mechanism of $Ag_3PO_4/SnSe_2$ composite photocatalyst under visible light irradiation.

The band structure of the $Ag_3PO_4/SnSe_2$ composite is plotted in Fig. 12. Under visible light irradiation, both Ag_3PO_4 and $SnSe_2$ could be excited to produce electrons and holes simultaneously due to their visible light response. In general, according to the double charge transfer theory [44], the photo-generated electrons of $SnSe_2$ would transfer to the CB of Ag_3PO_4 and the holes of Ag_3PO_4 would migrate to the VB of $SnSe_2$ with the reason that the VB and CB potentials of Ag_3PO_4 were both lower than those of $SnSe_2$. In this case, the electrons in the CB of Ag_3PO_4 and the holes in VB of $SnSe_2$ were effective in decomposing dyes. Actually, the photo-generated electrons in the CB of Ag_3PO_4 could not combine with O_2 to generate $\bullet O_2^-$ because the CB potential of Ag_3PO_4 was lower than $O_2/\bullet O_2^-$ redox couple (+0.13 eV/vs. NHE). Besides, the oxidation ability of h^+ located at the VB of $SnSe_2$ (1.12 eV vs. NHE) is too weak to decompose dyes. These were not consistent with the fact that h^+ and $\bullet O_2^-$ were the major active species in this system.

On the basis of the above experimental results and analysis, a possible Z-scheme photocatalytic mechanism was proposed to explain the enhanced stability and photodegradation efficiency for RhB. After introducing $SnSe_2$, the electrons in the CB of Ag_3PO_4 could easily transfer to the VB of $SnSe_2$ and combine with holes there. The electrons in the CB of $SnSe_2$ could react with O_2 to form $\bullet O_2^-$ radicals, and then oxidize RhB, while the holes in the VB of Ag_3PO_4 could directly oxidize the organic dyes. The scheme mechanism enabled the efficient separation of photo-generated charge carriers and was responsible for the improvement of photoactivity

and stability. The following equations were used to describe the possible reaction process of photodegradation for RhB.

$$Ag_3PO_4/SnSe_2 + hv \rightarrow Ag_3PO_4/SnSe_2(h^+ + e^-) \tag{1}$$

$$Ag_3PO_4(e^-) + SnSe_2(h^+) \rightarrow Ag_3PO_4 + SnSe_2 \tag{2}$$

$$e^-(SnSe_2) + O_2 \rightarrow \bullet O_2^- \tag{3}$$

$$\bullet O_2^- + RhB \rightarrow Products \tag{4}$$

$$h^+(Ag_3PO_4) + RhB \rightarrow Products \tag{5}$$

4. Conclusions

In summary, a series of novel $Ag_3PO_4/SnSe_2$ composites with different $SnSe_2$ content were successfully prepared. The as-prepared $Ag_3PO_4/SnSe_2$ composites showed an improved photocatalytic performance for degradation of RhB than pure Ag_3PO_4 and $SnSe_2$ under visible light. The composite with $SnSe_2$ content of 6 wt% exhibited the highest photocatalytic activity and displayed a better stability than pure Ag_3PO_4. Radical trapping experiments indicated that the enhanced activity of the composites could be attributed to the strong oxidizing ability of the $\bullet O_2^-$ species derived from the electrons in the CB of $SnSe_2$ and holes in the VB of Ag_3PO_4. The photocatalytic process is consistent with the Z-scheme photocatalytic mechanism. This study demonstrates that the $Ag_3PO_4/SnSe_2$ composite is a promising candidate for environmental pollution remediation and gives an idea to design other novel and highly efficient visible light driven photocatalysts by use of $SnSe_2$.

Appendix A. Supplementary data

Supplementary data associated with this article can be found, in the online version, at http://dx.doi.org/10.1016/j.apcatb.2016.09.033.

References

[1] D.J. Martin, G. Liu, S.J.A. Moniz, Y. Bi, A.M. Beale, J. Ye, J. Tang, Chem. Soc. Rev. 44 (2015) 7808–7828.
[2] Y.Q. Qu, X.F. Duan, Chem. Soc. Rev. 42 (2013) 2568–2580.
[3] Y. Wu, M. Xu, X. Chen, S. Yang, H. Wu, J. Pan, X. Xiong, Nanoscale 8 (2016) 440–450.
[4] B. Zhou, S. Yang, W. Wu, L. Sun, M. Lei, J. Pan, X. Xiong, CrystEngComm 16 (2014) 10863–10869.
[5] X. Chen, B.H. Zhou, S.L. Yang, H.S. Wu, Y.X. Wu, L.D. Wu, J. Pan, X. Xiong, RSC Adv. 5 (2015) 68953–68963.
[6] X. Chen, H. Li, H. Wu, Y. Wu, Y. Shang, J. Pan, X. Xiong, Mater. Lett. 172 (2016) 52–55.
[7] Y. Wang, X. Cheng, X. Meng, H. Feng, S. Yang, C. Sun, J. Alloys Compd. 632 (2015) 445–449.
[8] W. Zhao, Y. Guo, Y. Faiz, W.-T. Yuan, C. Sun, S.-M. Wang, Y.-H. Deng, Y. Zhuang, Y. Li, X.-M. Wang, H. He, S.-G. Yang, Appl. Catal. B-Environ. 163 (2015) 288–297.
[9] C. Yu, G. Li, S. Kumar, K. Yang, R. Jin, Adv. Mater. 26 (2014) 892–898.
[10] D. Xu, B. Cheng, S. Cao, J. Yu, Appl. Catal. B-Environ. 164 (2015) 380–388.
[11] Y. Bi, S. Ouyang, N. Umezawa, J. Cao, J. Ye, J. Am. Chem. Soc. 133 (2011) 6490–6492.
[12] F. Teng, Z.L. Liu, A. Zhang, M. Li, Environ. Sci. Technol. 49 (2015) 9489–9494.
[13] S.S. Patil, D.R. Patil, S.K. Apte, M.V. Kulkarni, J.D. Ambekar, C.-J. Park, S.W. Gosavi, S.S. Kolekar, B.B. Kale, Appl. Catal. B: Environ. 190 (2016) 75–84.

[14] X. Hua, F. Teng, Y. Zhao, J. Xu, C. Xu, Y. Yang, Q. Zhang, S. Paul, Y. Zhang, M. Chen, X. Zhao, Water Res. 81 (2015) 366–374.
[15] S.N. Zhang, S.J. Zhang, L.M. Song, Appl. Catal. B-Environ. 152 (2014) 129–139.
[16] C.-T. Dinh, T.-D. Nguyen, F. Kleitz, T.-O. Do, Chem. Commun. 47 (2011) 7797.
[17] Z.B. Jiao, Y. Zhang, H.C. Yu, G.X. Lu, J.H. Ye, Y.P. Bi, Chem. Commun. 49 (2013) 636–638.
[18] J. Wang, F. Teng, M.D. Chen, J.J. Xu, Y.Q. Song, X.L. Zhou, CrystEngComm 15 (2013) 39–42.
[19] P.Y. Dong, Y.H. Wang, H.H. Li, H. Li, X.L. Ma, L.L. Han, J. Mater. Chem. A 1 (2013) 4651–4656.
[20] W.C. Peng, X. Wang, X.Y. Li, Nanoscale 6 (2014) 8311–8317.
[21] T.Y. Huang, Y.J. Chen, C.Y. Lai, Y.W. Lin, RSC Adv. 5 (2015) 43854–43862.
[22] Z.-M. Yang, G.-F. Huang, W.-Q. Huang, J.-M. Wei, X.-G. Yan, Y.-Y. Liu, C. Jiao, Z. Wan, A. Pan, J. Mater. Chem. A 2 (2014) 1750–1756.
[23] R. Shao, X. Zeng, Z. Cao, H. Dong, L. Wang, F. Wang, J. Liu, Z. Li, Q. Liang, RSC Adv. 5 (2015) 102101–102107.
[24] J. Tang, W. Gong, T. Cai, T. Xie, C. Deng, Z. Peng, Q. Deng, RSC Adv. 3 (2013) 2543–2547.
[25] Q.J. Xiang, D. Lang, T.T. Shen, F. Liu, Appl. Catal. B-Environ. 162 (2015) 196–203.
[26] L. Wang, Y.Y. Chai, J. Ren, J. Ding, Q.Q. Liu, W.L. Dai, Dalton Trans. 44 (2015) 14625–14634.
[27] Y.H. Song, Y.C. Lei, H. Xu, C. Wang, J. Yan, H.Z. Zhao, Y.G. Xu, J.X. Xia, S. Yin, H.M. Li, Dalton Trans. 44 (2015) 3057–3066.
[28] P.Y. Ma, H.J. Yu, Y. Yu, W.M. Wang, H. Wang, J.Y. Zhang, Z.Y. Fu, Phys. Chem. Chem. Phys. 18 (2016) 3638–3643.
[29] C.N. Tang, E.Z. Liu, J. Fan, X.Y. Hu, Y.N. Ma, J. Wan, RSC Adv. 5 (2015) 91979–91987.
[30] S. Kumar, T. Surendar, A. Baruah, V. Shanker, J. Mater. Chem. A 1 (2013) 5333–5340.
[31] S.G. Meng, X.F. Ning, T. Zhang, S.F. Chen, X.L. Fu, Phys. Chem. Chem. Phys. 17 (2015) 11577–11585.
[32] P. Ramasamy, P. Manivasakan, J. Kim, CrystEngComm 17 (2015) 807–813.
[33] X. Zhou, L. Gan, W.M. Tian, Q. Zhang, S.Y. Jin, H.Q. Li, Y. Bando, D. Golberg, T.Y. Zhai, Adv. Mater. 27 (2015) 8035–8041.
[34] Y. Huang, K. Xu, Z.X. Wang, T.A. Shifa, Q.S. Wang, F. Wang, C. Jiang, J. He, Nanoscale 7 (2015) 17375–17380.
[35] C.F. Du, J.R. Li, X.Y. Huang, RSC Adv. 6 (2016) 9835–9842.
[36] Z. Fang, S.H. Hao, L.Y. Long, H. Fang, T.T. Qiang, Y.X. Song, CrystEngComm 16 (2014) 2404–2410.
[37] X. Yu, J. Zhu, Y. Zhang, J. Weng, L. Hu, S. Dai, Chem. Commun. 48 (2012) 3324–3326.
[38] C. Zhang, H. Yin, M. Han, Z. Dai, H. Pang, Y. Zheng, Y.-Q. Lan, J. Bao, J. Zhu, ACS Nano 8 (2014) 3761–3770.
[39] W. Wang, H.B. Fang, Y.Z. Zheng, Y. Che, X. Tao, J.F. Chen, RSC Adv. 5 (2015) 62519–62526.
[40] M. Sun, Q. Yan, T. Yan, M.M. Li, D. Wei, Z.P. Wang, Q. Wei, B. Du, RSC Adv. 4 (2014) 31019–31027.
[41] B. Wang, W. An, L. Liu, W. Chen, Y. Liang, W. Cui, RSC Adv. 5 (2015) 3224–3231.
[42] W.-K. Jo, J.Y. Lee, T.S. Natarajan, Phys. Chem. Chem. Phys. 18 (2016) 1000–1016.
[43] S.B. Kale, R.S. Kalubarme, M.A. Mahadadalkar, H.S. Jadhav, A.P. Bhirud, J.D. Ambekar, C.-J. Park, B.B. Kale, Phys. Chem. Chem. Phys. 17 (2015) 31850–31861.
[44] X. Chen, H. Li, Y. Wu, H. Wu, L. Wu, P. Tan, J. Pan, X. Xiong, J. Colloid Interface Sci. 476 (2016) 132–143.
[45] X. Chen, P. Tan, B. Zhou, H. Dong, J. Pan, X. Xiong, J. Alloys Compd. 647 (2015) 456–462.
[46] Y.Y. Chai, L. Wang, J. Ren, W.L. Dai, Appl. Surf. Sci. 324 (2015) 212–220.
[47] J. Wan, L. Sun, J. Fan, E.Z. Liu, X. Hu, C.N. Tang, Y.C. Yin, Appl. Surf. Sci. 355 (2015) 615–622.
[48] J. Choi, J. Jin, I.G. Jung, J.M. Kim, H.J. Kim, S.U. Son, Chem. Commun. 47 (2011) 5241–5243.
[49] Z. Wang, Y. Huang, W. Ho, J. Cao, Z. Shen, S.C. Lee, Appl. Catal. B: Environ. 199 (2016) 123–133.
[50] Y.Q. Wang, X.F. Cheng, X.T. Meng, H.W. Feng, S.G. Yang, C. Sun, J. Alloys Compd. 632 (2015) 445–449.
[51] H. Huang, K. Xiao, Y. He, T. Zhang, F. Dong, X. Du, Y. Zhang, Appl. Catal. B: Environ. 199 (2016) 75–86.
[52] J. Yang, R.S. Hu, W.W. Meng, Y.F. Du, Chem. Commun. 52 (2016) 2620–2623.
[53] L. Liu, Y.H. Qi, J.R. Lu, S.L. Lin, W.J. An, Y.H. Liang, W.Q. Cui, Appl. Catal. B-Environ. 183 (2016) 133–141.
[54] Z.H. Chen, F. Bing, Q. Liu, Z.G. Zhang, X.M. Fang, J. Mater. Chem. A 3 (2015) 4652–4658.
[55] N. Mohaghegh, M. Tasviri, E. Rahimi, M.R. Gholami, RSC Adv. 5 (2015) 12944–12955.
[56] X.F. Yang, J.L. Qin, Y. Jiang, K.M. Chen, X.H. Yan, D. Zhang, R. Li, H. Tang, Appl. Catal. B-Environ. 166 (2015) 231–240.
[57] Y.Y. Chai, J. Ding, L. Wang, Q.Q. Liu, J. Ren, W.L. Dai, Appl. Catal. B-Environ. 179 (2015) 29–36.